Programming multiconfiguration into bistable robots via traversable energy landscapes

Xin Tong[1, †], Qinghua Yu[2,3,†], Tianle Zhang[1,4], Chengru Jiang[2,3], Yangkang Jiang[5], Yang Yang[4], Dong Wang[2,3], Guoying Gu[2,3,*], Yingtian Li[6,1,*]

[1]Shenzhen Institutes of Advanced Technology, Chinese Academy of Sciences, Shenzhen 518055, China.
[2]State Key Laboratory of Mechanical System and Vibration, School of Mechanical Engineering, Shanghai Jiao Tong University, Shanghai 200240, China.
[3]Shanghai Key Laboratory of Intelligent Robotics, Shanghai Jiao Tong University, Shanghai 200240, China.
[4]School of Automation, Nanjing University of Information Science and Technology, Nanjing 210044, China.
[5]School of Control Science and Engineering, Tongji University, Shanghai 201804, China.
[6]School of Science and Engineering, The Chinese University of Hong Kong, Shenzhen 518172, China.

***Corresponding authors. E-mails:** guguoying@sjtu.edu.cn; liyingtian@cuhk.edu.cn
†Equally contributed to this work.

ORIGINAL UNEDITED MANUSCRIPT

Downloaded from academic.oup.com/nsr/advance-article/doi/10.1093/nsr/nwag643/8917835 by Shanghai Jiao Tong University user on 23 October 2026

© The Author(s) 2026. Published by Oxford University Press on behalf of China Science Publishing & Media Ltd. This is an Open Access article distributed under the terms of the Creative Commons Attribution License (https://creativecommons.org/licenses/by/4.0/), which permits unrestricted reuse, distribution, and reproduction in any medium, provided the original work is properly cited.

ABSTRACT:
Soft robots using bistable structures often face limitations due to a fixed energy landscape, which restricts their configurational adaptability and functional diversity. To address this challenge, we introduce an energy-landscape-traversing (ELTra) bistable structure that enables on-demand reconstruction of the energy landscape, continuous stabilization of intermediate states, and precise modulation of energy release, capabilities that are challenging to achieve with conventional systems. Based on the established theoretical model of the ELTra bistable structure, we developed an ELTraBot prototype that features four distinct configurations, including two intermediate-stable configurations absent in traditional bistable structures. We further demonstrated the ELTraBot's remarkable versatility, allowing it to perform nine distinct functions by leveraging its reconfigurable states. This design reduces the need for complex dedicated hardware and significantly simplifies design. Our work establishes a new design method for multifunctional, reconfigurable robots by advancing beyond binary bistability into the realm of continuously programmable materials.

Keywords: bistable structure, energy landscape reconstruction, controllable energy release, intermediate states stabilization, reconfigurable robot.

INTRODUCTION

Soft robotics represents an exciting frontier research area, due to its unique ability to mimic natural forms and adapt to diverse environments [1,2]. However, a significant challenge within the field is the trade-off between deformability and response speed [2,3], primarily resulting from the viscoelastic properties of soft materials and the inherent delays of actuation mechanisms [4,5]. Bistable soft robots have emerged as a promising solution to address this issue by leveraging the rapid energy release through transitions between two stable states [6–8]. By harnessing mechanical instabilities [9,10] and programming intermediate states [11,12], they enable efficient locomotion [13–15], rapid actuation [16,17] and robust mechanical responses [18,19] that are otherwise difficult to achieve with conventional soft actuators. As a result, researchers have widely explored bistability to enhance the adaptability, agility, and sensitivity of soft robotic systems.

Despite these advantages, conventional bistable structures have fixed energy landscapes defined during fabrication, and their actuation control, energy regulation, and instability triggering remain fixed throughout operation, fundamentally limiting their versatility: performance cannot be adjusted in real time or across multiple modes. Among the possible solutions, tendon-driven systems offer high response speed that complements the rapid energy release of bistable structures [10,20]. These systems can also achieve zero stiffness under compression, allowing full energy release without altering the energy barrier. However, these systems apply forces acting in a single direction, resulting in under-actuation [21,22]. In contrast, fluidic actuators provide adaptive and real-time controllable force output [23,24], making them more suitable for triggering bistable transitions [25,26]. Yet, soft fluidic actuators tend to dampen the structure's sudden snap-through behavior due to their viscous resistance. Thus, it remains challenging to preserve the structure's inherent bistability while simultaneously exhibiting on-demand tunable properties: (i) real-time energy-landscape reconstruction, which is defined as the actuation-induced reshaping of the energy landscape; (ii) continuous stabilization of intermediate states, meaning the quasi-static stabilization of the structure's configurations between the two intrinsic stable states; and (iii) post-snap-through energy-release control, which regulates the energy and response after snap-through.

ORIGINAL UNEDITED MANUSCRIPT

Downloaded from academic.oup.com/nsr/advance-article/doi/10.1093/nsr/nwag643/8917835 by Shanghai Jiao Tong University user on 23 October 2026

Herein, we present a new type of bistable structure that expands the typical controllable curve of bistable systems to continuous, reversible, energy-landscape-traversal control regions; hence, it is named the ELTra bistable structure, as described in Fig. 1A. The design features a centrally symmetric bistable shell [27–29] sandwiched between two air pouches. The pouches deliver uniform and effective pressure across the bistable shell surface and provide high stiffness along one direction, thereby initiating transitions while preserving the bistable configurations. Specifically, the bottom uniform air pouch (UAP) reshapes the global energy landscape, whereas the top orthogonalized air pouch array (OAA) stabilizes intermediate states and triggers state transitions through localized pneumatic loading (Fig. S1 and Fig. S2). By coordinating the actuation of both pouches, the structure further enables energy landscape traversal control, allowing continuous and reversible tuning of the energy within the varied reconstructed energy landscapes (Fig. 1B), which is discussed in the next section. To realize programmable behaviors, a theoretical model based on minimum potential energy is established to predict the bistable morphologies and energy landscape under varying geometries and pressures, thereby providing a quantitative framework for controlled switching. The model further calculated the energy barrier to predict the pneumatic pressure required to either stabilize intermediate states or trigger transitions in both the original and reconstructed energy landscapes, providing a quantitative tool for programming behaviors.

Building on the ELTra bistable structure, this study developed a bistable robot by elongating the bistable sandwich units along their long-edge direction and localizing the orthogonal air-pouch array into two orthogonal air pouches (OAP) positioned on the left and right (l-OAP and r-OAP) sides of the robot (Fig. 1A). The proposed robot enables localized snap-through in specific segments. This feature introduces two additional configurations and significantly enhances shape adaptability and locomotion versatility beyond the rapid transitions between stable states demonstrated in prior works. Since this robot features an elongated ELTra bistable structure with flexible transitioning configurations, it is named ELTraBot (Fig. 1C).

We demonstrate its enhanced and programmable behaviors by utilizing the three types of snap-through properties as illustrated in Fig. 1D. The first is the Full-Energy Transition Mode. Within the mode, the structure is either locked in a stable state or undergoes a complete, rapid switch. The functions include rolling, direct jumping, deployment, and self-protection. The second is the Partial-Instability Regulation Mode. These functions utilize the tunability of intermediate states to partially regulate the structure's energy. Selective jumping, cooperative transportation, and hooking belong to this mode. The last one is the Non-Snap-Through Morphing Mode. These functions operat e entirely outside the snap-through regime, relying solely on the continuous elastic deformation of the shell without triggering any instability. This mode covers crawling and multi-modal grasping.

We also prepared a comparison table (Supplementary Table 1) that contrasts our ELTraBot with prior works on key metrics. Our ELTra structure advances energy landscape reconstruction and intermediate state tunability, resulting in four configurations and nine functions of the ELTraBot, compared to prior works that typically show only two configurations with fixed energy landscapes. Overall, our work unlocks continuous and programmable control over an expanded range of states beyond traditional bistable systems and establishes a new design method for multifunctional, reconfigurable soft robots.

ORIGINAL UNEDITED MANUSCRIPT

Downloaded from academic.oup.com/nsr/advance-article/doi/10.1093/nsr/nwag643/8917835 by Shanghai Jiao Tong University user on 23 October 2026

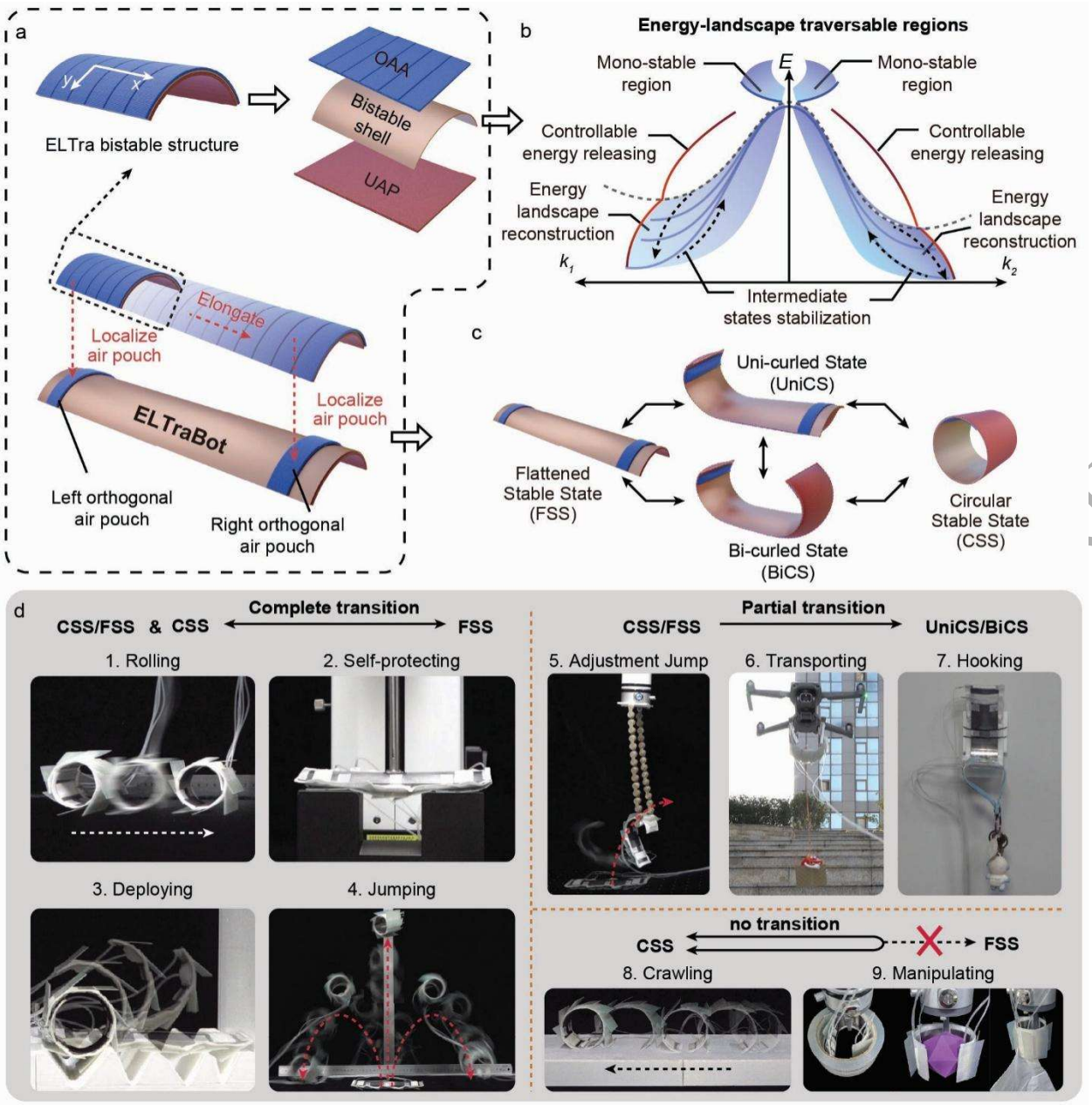


Figure 1. The design of our proposed bistable structure and its robotic application. (A) The design of the proposed ELTra bistable structure and ELTraBot. (B) The conceptual illustration of the continuous, reversible, and traversable energy landscapes of the proposed bistable structure. (C) The robot's four distinct and transformable configurations. (D) Summary of the robot's functions based on its varied configurations and transitions, including those at FSS (Flattened Stable State) and CSS (Circular Stable State), as well as the complete, partial, and no transition processes from FSS or CSS to the UniCS (Uni-side Curled State) and BiCS (Bi-side Curled State).

RESULTS AND DISCUSSION

The energy-landscape-traversal bistable robot

ELTra bistable structure element

The ELTra bistable structure introduced in this work features a sandwich form of three

ORIGINAL UNPT

Downloaded from academic.oup.com/nsr/advance-article/doi/10.1093/nsr/nwag643/8917835 by Shanghai Jiao Tong University user on 23 October 2026

functional layers (Fig. 1A): a bottom uniform air pouch (UAP), a top orthogonal air-pouch array (OAA), which comprises serially connected air pouches oriented orthogonally to the long edge of the UAP, and a middle cylindrical shell bistable structure (referred to as the bistable shell). The bistable shell serves as the core mechanical component, shaping the energy landscape of the bistable shell and providing two distinct shapes, i.e., stable state 1 (SS1) and stable state 2 (SS2). They are theoretically represented [30,31] by the black dashed curve in the coordinate system of Fig. 2A.

Actuation is achieved through the flexible, inextensible fabric air pouches [32,33] which reconstruct the shell's overall shape and trigger snap-through transitions between stable states. A detailed introduction to this type of air pouch can be found in Supplementary Note 1 and Figs. S1 and S2. Building upon these design insights, we present continuous and reversible actuation methods to manipulate the ELTra bistable structure (Fig. 2A). The continuous transition from SS1 to SS2 occurs as follows: first, the UAP is inflated and held constant to increase the bistable shell curvature, which effectively reconstructs its energy landscape (red dashed line of Fig. 2A-II). Next, the pressure in the OAA is gradually increased, which reduces structural curvature and lowers the energy barrier to stabilize the intermediate state along the newly constructed energy landscape until a critical state is reached, triggering snap-through (blue solid line of Fig. 2A-III). Finally, deflation of both UAP and OAA restores the system to the SS2 configuration. Reversing this sequence allows the inverse transition from SS2 back to SS1 (Fig. 2A-i to Fig. 2A-iii).

Regarding the actuation methods, we provide a systematic illustration in Supplementary Note 2 and Fig. S3-S4. The control of the ELTra bistable system is divided into two modes. Small-scale energy control: a small amount of air is injected into the UAP without generating initial pressure, so the initial energy barrier remains unchanged. In this case, the structure is driven solely by the OAA to cross this critical point. After snap-through, the compressed air trapped in the UAP cavity generates pressure that counteracts deformation, enabling partial regulation of the released energy. Large-scale energy control: a larger volume of air is injected to generate an initial pressure, which lifts and broadens the left-side energy barrier. Once the OAA drives the structure to cross the critical point, the cavity pressure continues to rise, strongly suppressing deformation and allowing extensive regulation of the released energy. Accordingly, whether an initial pressure is generated or not, these two strategies correspond to volume-controlled and pressure-controlled regulation, respectively. Based on the above actuation schemes, we further establish a framework to enable continuous actuation and transition between the two stable states. Specifically, the theory of the configuration and energy characterization of the ELTra bistable structure, together with its experimental validation, is described below.

Analysis and characterization of the ELTra bistable structure

In this section, we analyze the deformation mechanism of the ELTra bistable structure based on the principle of minimum potential energy [34–36]. The bistable shell serves as the primary carrier of mechanical energy, motivating us to theoretically model and analyze its energy landscape. We begin by considering a bistable shell with width W and thickness H that exhibits bistable behavior (Fig. 2B). The energy density Π of the bistable shell can be expressed as a function of the curvature k_1 and k_2. By minimizing Π, the stable states of the bistable shell can be obtained. The detailed calculation of the energy density can be found in Supplementary Note 3-5, and Figs. S5, S6, and S7.

ORIGINAL UNEDITED MANUSCRIPT

Downloaded from academic.oup.com/nsr/advance-article/doi/10.1093/nsr/nwag643/8917835 by Shanghai Jiao Tong University user on 23 October 2026

Next, we conducted a series of experiments to verify the relationship between curvature and air pressure in the UAP or OAA, which is critical for energy landscape reconstruction and intermediate state stabilization. As illustrated in Fig. 2B, when the bistable structure is in SS1 ($k_1 \neq 0$). The experimental results indicate that increasing air pressure within the UAP leads to a rise in the curvature k_1 (as shown in the top panel of Fig. 2B), enhancing

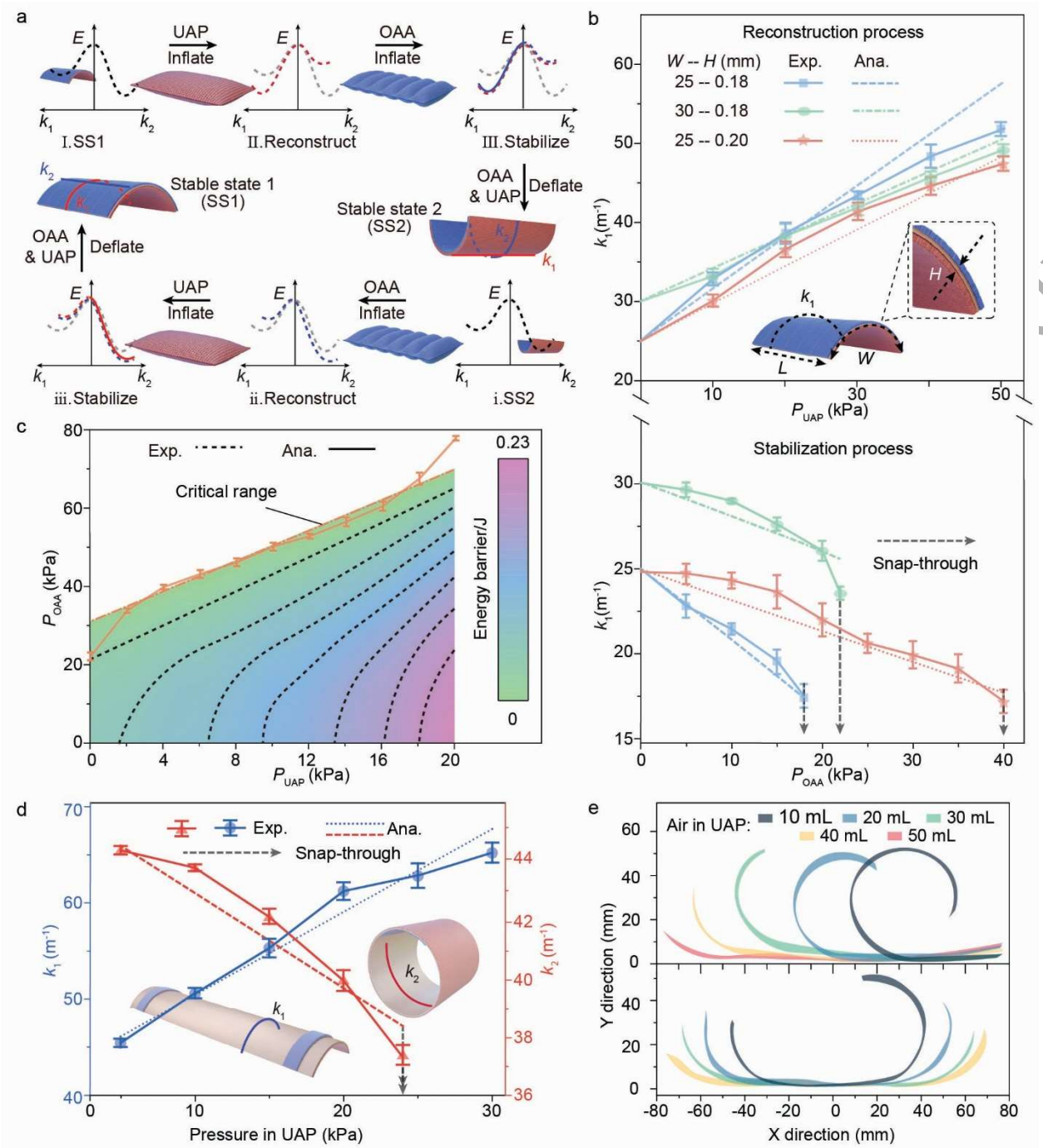


Figure 2. An analysis of the ELTra bistable structure and our proposed robot. (A) The complete transition processes between the two stable states. In the coordinate system, the dashed lines correspond to the reconstruction of the energy landscape, while the solid lines represent the stabilization of intermediate states along the newly constructed energy landscape and the triggering of snap-through behavior. (B) The theoretical results and their verification regarding the deformation of curvature k_1 and k_2 under the independent actuation of UAP or OAA. (C) The calculated energy achieved through the combination of the two air pouches and the verification of

Downloaded from academic.oup.com/nsr/advance-article/doi/10.1093/nsr/nwag643/8917835 by Shanghai Jiao Tong University user on 23 October 2026

the predicted critical pressure. (D) The theoretical verification of the ELTraBot's curvature k_1 and k_2 under independent actuation of the UAP. (E) The configuration characterization of UniCS and BiCS of the robot.

the energy density Π in the system. Conversely, increasing the air pressure in the OAA decreases the curvature k_1 (as shown in the second subfigure of Fig. 2B), thereby lowering the energy barrier of the structure to stabilize its intermediate state and decreasing the trigger force as depicted in Fig. S8. When this energy barrier becomes sufficiently low, surpassing the critical state, the structure undergoes a snap-through. The close agreement between experimental data and theoretical predictions confirms that the proposed model accurately predicts the structural deformation behavior under individual actuation modes.

Since the bistable shell and the air pouches (UAP and OAP) are the key actuation components in this study, we have performed systematic cyclic fatigue tests on the bistable shell and comprehensive air-tightness evaluations of the pneumatic pouches, the results of which have been shown in Supplementary Note 6 and Fig. S9. These results confirm the excellent long-term reliability and robustness of both the bistable shell and the air pouches under conditions that exceed typical operational demands.

Finally, we analyzed the energy characteristics of the bistable structure under combined actuation of UAP and OAA (Supplementary Notes 7 and 8, and Fig. S10) and conducted a series of experimental validations. As illustrated in the contour map of Fig. 2C, when only the UAP is inflated ($P_{\mathrm{OAA}} = 0\,\mathrm{kPa}$), the energy barrier required to trigger instability increases, which will be proven in the next section on Robust self-protection. Maintaining the constant UAP pressure establishes a reconfigured energy landscape (red dashed line of Fig. S10). Subsequent inflation of the OAA enables precise modulation of the energy barrier to stabilize intermediate states along this reconstructed landscape. This is totally different from previous research that can only decrease the energy barrier along its fixed energy landscape [37–40]. The dashed lines in Fig. 2C indicate that for any energy landscape reconstructed by a given UAP pressure, adjusting the OAA pressure can tune the energy barrier to a consistent level within the entire reconstructed energy landscape.

The highlighted orange line within the green region denotes the critical energy barrier corresponding to the instability threshold, with its horizontal and vertical coordinates representing the OAA pressure required to induce snap-through. As direct quantification of the structure's internal energy is challenging, we conducted the trigger pressure experiment, and the results confirm that the pressure thresholds for triggering instability align closely with theoretical predictions. Together, these analyses and experimental findings lay a theoretical foundation for establishing an energy landscape traversal-controllable region in the sandwich bistable structure.

Characterization of ELTraBot in four configurations

As described in Fig. 1C, our ELTra bistable robot (ELTraBot) exhibits four distinct configurations. To verify the applicability of the above theoretical model, we conducted a series of experiments to characterize the pneumatic-induced deformations across the four configuration states, utilizing a structurally optimized prototype. To enable ELTraBot's mobility, this study integrated a self-developed rolling actuator along with its self-locking mechanism. The details of ELTraBot's structure can be found in Supplementary Notes 9-12 and Figs. S11-13.

ORIGINAL UNEDITED MANUSCRIPT

Downloaded from academic.oup.com/nsr/advance-article/doi/10.1093/nsr/nwag643/8917835 by Shanghai Jiao Tong University user on 23 October 2026

Utilizing the prototype, we first present the curvature changes of k_1 and k_2 induced by the actuation of UAP as shown in Fig. 2D. The experimental results align well with previously established theoretical predictions. Notably, the test for k_2 was halted at the instability threshold of 24 kPa, beyond which the system rapidly transitions to FSS. Our observations indicate that this snap-through occurs when a localized section of the structure buckles, increasing the volume of the air pouch and elevating the potential energy of the local air pressure.

We then experimentally characterized the ELTraBot's configuration in UniCS and BiCS. By varying the inflation Volume of the UAP, we tested the geometric configurations of the robot to determine the critical air volume (Fig. 2E), within which the robot can maintain its configuration of UniCS or BiCS. The upper and lower critical volumes for BiCS are 10 and 40 mL, respectively, while for UniCS, the values are 10 mL and 50 mL. Below the lower critical pressure, the robot buckles into its circular stable state (CSS), while beyond the upper critical air volume, the robot deploys into the flattened stable state (FSS). We then characterized the relationship between air volume and pressure, and the pressure-volume hysteresis in each configuration. Fig. S14 shows a distinct U-shaped pressure-volume relationship, with the minimum pressure occurring around 20 mL inflation. The hysteresis results (Fig. S15) show a descending trend in the first and third stages but an ascending trend in the second stage. These results will be discussed in Supplementary Note 13.

We also notice that the bistable shell's aspect ratio influences the configuration behaviour. To quantify this, we fabricated and tested a set of prototypes with identical material properties and shell thickness, while varying the shell width and length. The experimental results show a clear monotonic dependence, i.e., as the shell width increases, the critical aspect ratio decreases. The detailed experimental design and its results can be found in Supplementary Note 13 and Fig. S16.

Functions of the ELTraBot

Building on the traversable energy landscape proposed above, this section adopts the four distinct configurations of ELTraBot and their transitions to demonstrate their effectiveness in various functional applications and to reveal the energy characteristics during the actuation process of each function. There are four types of transitions: (1) Transition between two stable states of the robot. (2) Transition between UniCS and Stable States. (3) Transition between BiCS and Stable States. (4) Transition between UniCS and BiCS. The detailed actuation methods for these four transition types are illustrated in Supplementary Note 14 and Fig. S17. In total, 11 idealized actuation methods are derived from the combinations of these transitions, each detailed in Fig. S18. By leveraging the multiple achievable configurations within a single robot and the transition methods among them, our robot is endowed with nine distinct functions, which are categorized into three types as outlined in the introduction. To provide a clearer overview of the ELTra mechanism and ELTraBot, and to clarify the relationships among functions, we present Fig. S19, which summarizes the three categories of functions, the nine functions, the four configurations, the four transition types, and the corresponding actuation methods. These will be introduced in detail below, with their quantitative performance characterization summarized in Supplementary Note 15 and Table S2.

Demonstrating the functions of CSS, FSS, and their complete transition

Velocity-tunable rolling: The cylindrical configuration (Fig. 3A) in CSS offers an inherent

ORIGINAL UNEDITED MANUSCRIPT

Downloaded from academic.oup.com/nsr/advance-article/doi/10.1093/nsr/nwag643/8917835 by Shanghai Jiao Tong University user on 23 October 2026

structural advantage for achieving rolling locomotion, a highly effective locomotion strategy commonly employed in various technological applications [41,42]. To secure the cylindrical configuration, we used a self-locking mechanism to prevent unintended deployment (Fig. S12). During the pneumatic actuation of the rolling actuator, the energy landscape of ELTraBot is reconstructed to a vertical line, as shown in the right corner of Fig. 3A. This landscape indicates that the structure of the robot remains in its CSS while the energy can be enhanced by inflating the rolling actuator. This occurs because of the self-locker

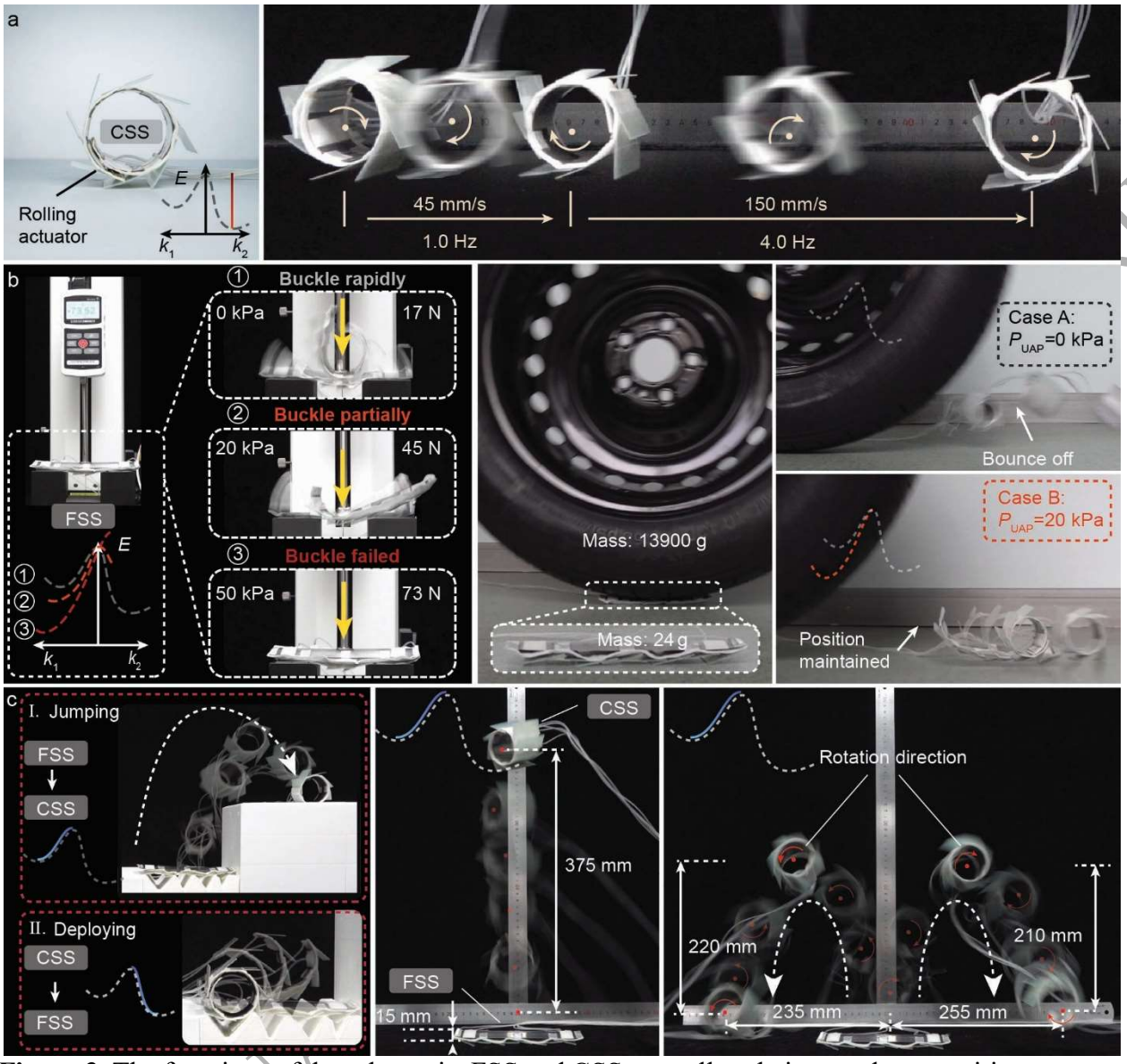


Figure 3. The functions of the robot at its FSS and CSS, as well as their complete transition process. (A) Rolling at CSS: the ELTraBot at CSS naturally performs rolling locomotion, utilizing a self-locking mechanism to reconstruct a new energy landscape of a vertical line (left). Variable velocity rolling is achieved by tuning the actuation frequencies (right). (B) Self-protection at FSS: Inflation of the UAP stabilizes the FSS by reconstructing its energy landscape into a more stable state, even a monostable one, as demonstrated by the compression tests (left). An impulsive loading assessment using a tire is also conducted (right). (C) Deployment and jumping during the transitions between FSS and CSS: the switch from FSS to CSS enables jumping (I), while the reverse transition

ORIGINAL MANUSCRIPT

Downloaded from academic.oup.com/nsr/advance-article/doi/10.1093/nsr/nwag643/8917835 by Shanghai Jiao Tong University user on 23 October 2026

facilitates deployment (II). Their combination allows for trap escape, with both vertical and bi-directional jumping demonstrated by varying the OAP actuation sequence.

prevents the robot from transitioning to its flattened configuration yet allows external actuation to accumulate strain energy within the circular configuration. The right panel illustrates the robot's rolling performance, where adjusting actuation frequency enables variable velocities on the ground (Fig. S20 and Supplementary Movie S1). Detailed explanations of the control strategy for rolling locomotion are provided in Supplementary Note 10.

Robust self-protection: Clearly, the flattened configuration in FSS exhibits greater resistance to loading compared to the vulnerable circular configuration in CSS, enhancing the robot's self-protection capability [43,44]. Our investigation reveals that UAP inflation reconstructs the energy landscape (Fig. 2A, Figs S3B and S8), resulting in a substantially wider and higher energy landscape than that of the initial state. This reconstruction requires greater energy input to overcome the energy barrier and trigger snap-through, while reducing the energy released after triggering relative to the baseline configuration. Consequently, it enhances the structure's load-bearing capacity while minimizing its instability during snap-through.

Hence, we conducted the compression tests illustrated in the left panel of Fig. 3B. The data correlating triggering force and pressure in the UAP are presented in Fig. S21. Three typical tests, shown on the right side of the first panel of Fig. 3B, demonstrate a direct correlation between increased pressures and enhanced load-bearing capacity (Supplementary Movie S2). Notably, at 50 kPa, the Robot exhibited a remarkable load resistance of 73 N, which is 4.3 times its depressurized state. Meanwhile, the robot maintains its deployed configuration, indicating that the robot presents a mono-stable state.

We also performed an experiment to test the self-protection function in facing dynamic loading using a rolling tire weighing 13900 g to roll over the deployed robots (24 g), with one UAP maintained at ambient pressure (0 kPa) and the other pressurized to 20 kPa. The unpressurized robot rapidly ejected from the camera's field of view upon tire compression. In contrast, the 20 kPa pressurized ELTraBot maintained its structural stability and stayed at its initial position, enabling continuous forward rolling. These findings reveal that by programming the energy landscapes of the robot in FSS's flattened configuration, the robot exhibits remarkable impact resistance, withstanding dynamic loads up to 579 times its mass.

Deployment and Jumping: A complete configuration transition between FSS and CSS is leveraged in this section. The transition from FSS to CSS triggers an instantaneous release of substantial energy. This dynamic process is most visibly demonstrated by the robot's ability to jump, allowing it to effectively overcome obstacles [9,45]. Combined with the transition from CSS to FSS, which induces a deployment function, their combination endows the ELTraBot with the ability to overcome a trap and jump up to the obstacle (the left panel of Fig. 3C and Supplementary Movie S3).

Then, we systematically investigated the tri-directional jumping behaviors and dynamic characteristics achieved under different actuation combinations of the l-OAP and r-OAP. In the vertical jumping mode (the left panel of Fig. 3C), when both the l-OAP and r-OAP are simultaneously inflated to 150 kPa, the robot detaches from the ground almost instantaneously, transitioning rapidly from FSS to CSS. Experimental results show a

ORIGINAL UNEDITED MANUSCRIPT

Downloaded from academic.oup.com/nsr/advance-article/doi/10.1093/nsr/nwag643/8917835 by Shanghai Jiao Tong University user on 23 October 2026

vertical jump height of 375 mm, which is 25 times its initial height of 15 mm. For horizontal jumping (jumping left and right), directional jumps are accomplished by actuating only the OAP opposite the intended direction of travel, actuating the r-OAP for a leftward jump, and the l-OAP for a rightward jump. As illustrated in the right panel of Fig. 3C, the robot achieves a maximum horizontal jump distance of approximately 255 mm, accompanied by a peak jump height of 210 mm. Based on the experimental results, we further quantified the conversion efficiency from theoretically released structural energy (Supplementary Note 16) to the experimentally measured jumping energy. The calculations in Supplementary Note 16 show that the energy-conversion efficiencies are 8.94% for the vertical jumping and 5.63% for left and right jumping.

Utilizing the UniCS and BiCS through partial transition from FSS/CSS

Selective jumping: The UniCS configuration of our robot is realized by incrementally inflating the UAP, which reduces the snap-through energy release. To investigate selective jumping through the transition process from FSS to UniCS, we conducted a series of experiments, as illustrated in Fig. 4A and Supplementary Movie S4.

As reported in previous studies [7,14] the robot exhibits a measurable jumping rotation angle. As illustrated in the middle panel of Fig. 4A, this is defined as the angle between the upward vertical direction and the vector extending from the midpoint of the deployed robot to the geometric center of the curled portion. This parameter is important because the pneumatic inflation volume influences not only the jumping trajectory but also the post-launch posture of the robot, which can perform a J-shaped morphology suitable for attachment to overhead structures. By characterizing the robot's morphology, jumping trajectory, and rotation angle, we can predict the robot's in-air posture and thereby assess its ability to achieve successful attachment. The characterization results are presented in the left panel of Fig. 4A. These results show that a 5 mL pneumatic inflation enabled a jump distance and height approximately twice those achieved with a 20 mL inflation. In addition, larger pneumatic volumes reduce the rotational counts during in-air jumping and lead to different postures at the highest points and landing points (Fig. S22).

Based on these results, we design selective jumping demonstrations. The 10 mL inflation produced the maximum jump height and caused the robot to jump over the rescue ladder (the left panel of Fig. 4A), whereas a 15 mL charge achieved an appropriate trajectory and enabled stable attachment (the right panel of Fig. 4A). We further demonstrated dynamic attachment to horizontally moving ladders (Fig. S23).

Cooperative transportation with UAV: In this section, we designed a cooperative experimental demonstration with a UAV to validate the efficacy of the transition from FSS to BiCS. First, we conducted preliminary benchtop experiments examining robot attachment to UAV platforms (Supplementary Movie S5). When the UAP was not inflated, the ELTraBot released energy rapidly during the transition to its CSS's cylindrical configuration. This approach destabilized the UAV, which landed above the middle of the robot, resulting in attachment failure as shown in the left panel of Fig. 4B. Conversely, inflating a constant value of 30 mL of air into the UAP induces an internal air compression during the abrupt configuration transition, leading to a rapid pressure increase that dramatically reduces the released energy. Even with the UAV offset by 20 mm, experimental results remain consistent (Fig. S24: Case B-1). Notably, during UAV offset experiments at 30 mL air inflation, extending the time interval between l-OAP and r-OAP

ORIGINAL UNEDITED MANUSCRIPT

Downloaded from academic.oup.com/nsr/advance-article/doi/10.1093/nsr/nwag643/8917835 by Shanghai Jiao Tong University user on 23 October 2026

actuation from 0.7 s to 3 s allowed the robot to exhibit autonomous positional correction, harnessing released energy to gradually align the UAV (Fig. S24: Case B-2). At last, we conducted field experiments to validate the Robot's capability to attach to UAVs and transport objects without the requirement of continuous actuation in real-world operations (right panel of Fig. 4B).

Hooking objects: Finally, we examine the function when the robot is activated to transform from the configuration of CSS to that of UniCS or BiCS. To realize this transition process, it requires locally reconstructing the energy landscape where the OAP acts to secure the curling on the left or/and the right side while allowing the middle segments' transition to

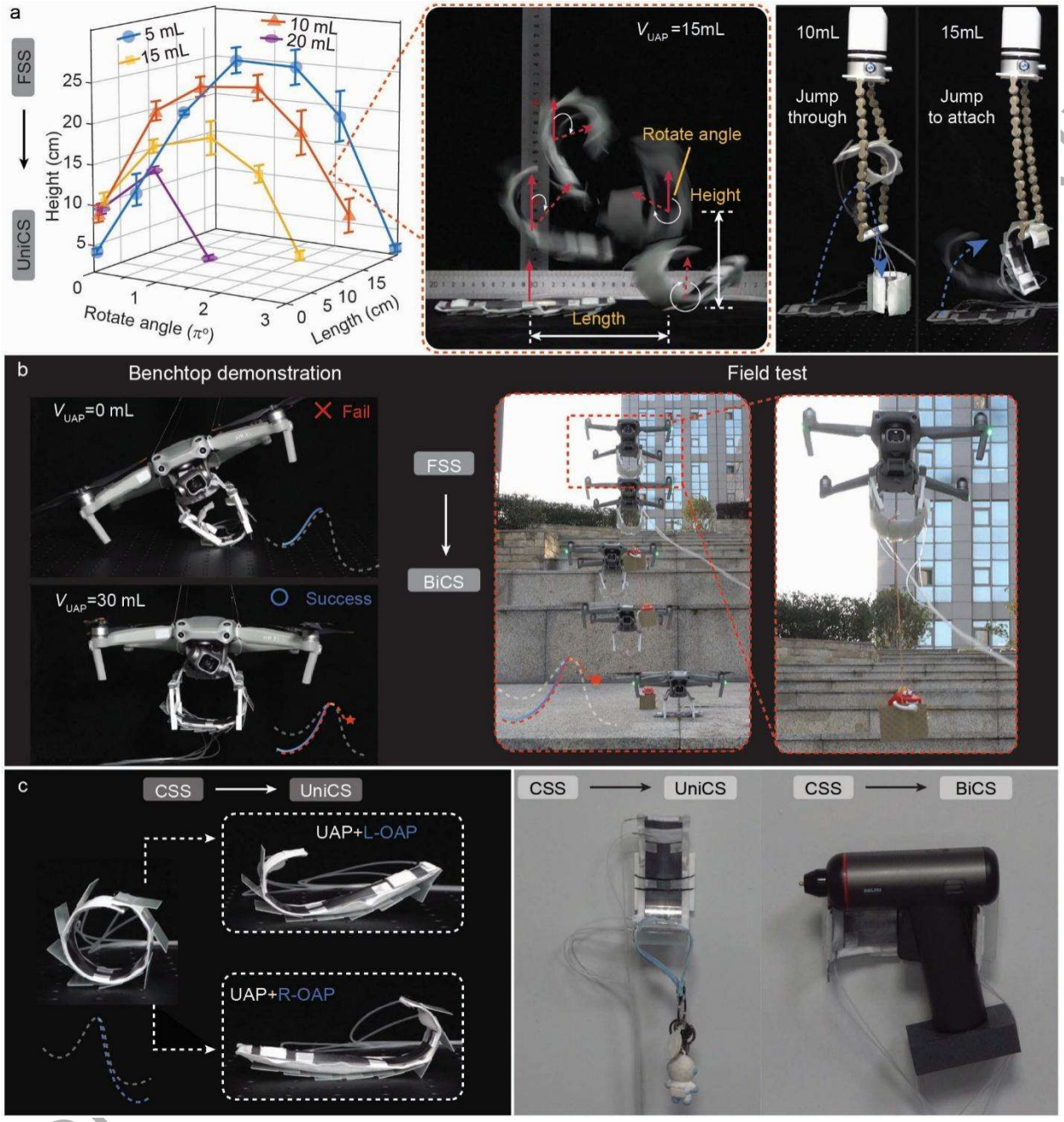


Figure 4. The function of the robot in its UniCS and BiCS configurations. (A) Selective jumping: By leveraging the partial transition from FSS to UniCS, the 3D graph (left) quantifies jump performance, while a typical jumping demonstration (middle) illustrates the motion. Selective

Downloaded from academic.oup.com/nsr/advance-article/doi/10.1093/nsr/nwag643/8917835 by Shanghai Jiao Tong University user on 23 October 2026

jumping utilizes the UniCS configuration to cross a ladder and to attach to it (right). (B) Cooperative transportation with UAV: A partial transition from FSS to BiCS enables the robot to function as an interactive carrier for UAV transportation. (C) Hooking objects: Starting from CSS, the robot can be induced to undergo a partial transition to either UniCS or BiCS, enabling it to hook objects.

deploy freely (left panel of Fig. 4C). Using this configuration, we design object-hooking experiments.

First, we conducted two benchtop tests based on the energy landscape control method, with results shown in the first panel of Fig. 4C (Supplementary Movie S6). By pre-pressurizing the l-OAP or r-OAP, the ELTraBot achieves selective curling on the activated side while permitting a flattened configuration of the opposite side. We then positioned the robot vertically and horizontally against a wall to hook various objects by single-sided or double-sided hooking, respectively. The demonstration proves that this partial energy-landscape enhancement strategy through OAP inflation enables the robot to perform selective local curling while other segments remain straight for effective hooking.

Leveraging the CSS deformation without inducing transition

Terrestrial crawling and multimodal gripping: The arc length along the curvature-2 (k_2) direction is significantly greater, approximately equal to the full perimeter of the CSS configuration, whereas deformation along the k_1 direction is constrained by the robot's width. This geometric difference allows extensive deformation along k_2 without inducing snap-through. Based on this, this section focuses on introducing the multifunctional applications, including crawling [46,47] and multimodal gripping [48,49], performed by the robot when undergoing uniform deformation along the k_2 direction from CSS.

During the crawling process, cyclic inflation and deflation of UAP create periodic energy fluctuations that align with air volume variations. This results in reciprocating modulation of the robot's crawling step starting from CSS (Fig. S25), enabling leftward locomotion (Fig. 5A). By integrating the previously demonstrated rolling function, our ELTraBot can achieve bidirectional locomotion (both forward and backward) through a hybrid locomotion strategy (Supplementary Movie S7).

We also demonstrated the gripping functionality of the ELTraBot, as depicted in Fig. 5B. Our robot operates in three gripping modes. (1) Pinch: For small contact dimensions, the robot uses low pneumatic pressure (0-10 kPa) to form a C-configuration, allowing it to pinch and catch objects like tissue paper (top panel of Fig. 5B). (2) Grasping: For larger objects, higher pressure (0 kPa, 20 kPa) is employed to deform the robot into a wider C-configuration, enabling it to grasp irregular-shape items like the shown in the middle panel of Fig. 5B. (3) Expanding to hold: For objects with even large outer dimensions but with inner cavities, a pressure of 30 kPa is used to outward-expand the robot, allowing it to press against the inner surfaces and lift the object through the friction generated. All gripping characterization and processes are detailed in Supplementary Note 17, Fig. S26, and Supplementary Movie S7.

CONCLUSIONS

This study introduces the ELTra bistable structure, a novel approach that redefines the controllability of bistable structures. Unlike previous research, which faced limitations in controllability and functionality due to the relatively fixed energy landscape, our solution

ORIGINAL UNEDITED MANUSCRIPT

Downloaded from academic.oup.com/nsr/advance-article/doi/10.1093/nsr/nwag643/8917835 by Shanghai Jiao Tong University user on 23 October 2026

effectively reconstructs the energy landscapes and tunes along them to trigger adjustable snap-through. This advancement expands the controllability of our ELTra bistable structure into continuous, reversible, and energy-landscape-traversal regions, in contrast to typical bistable structures that are limited to a single curve. Building on this, we construct a unique ELTraBot with four intrinsic configurations by elongating and modifying the ELTra bistable structure. By leveraging controllability, the robot can transform among the four configurations. We systematically developed a theoretical model to analyze energy changes and the control framework of the bistable structure, specifically focusing on its energy-landscape reconstruction, energy-release regulation, and energy-barrier tuning. This model serves as a guide for studying the characteristics of the bistable robot across its four

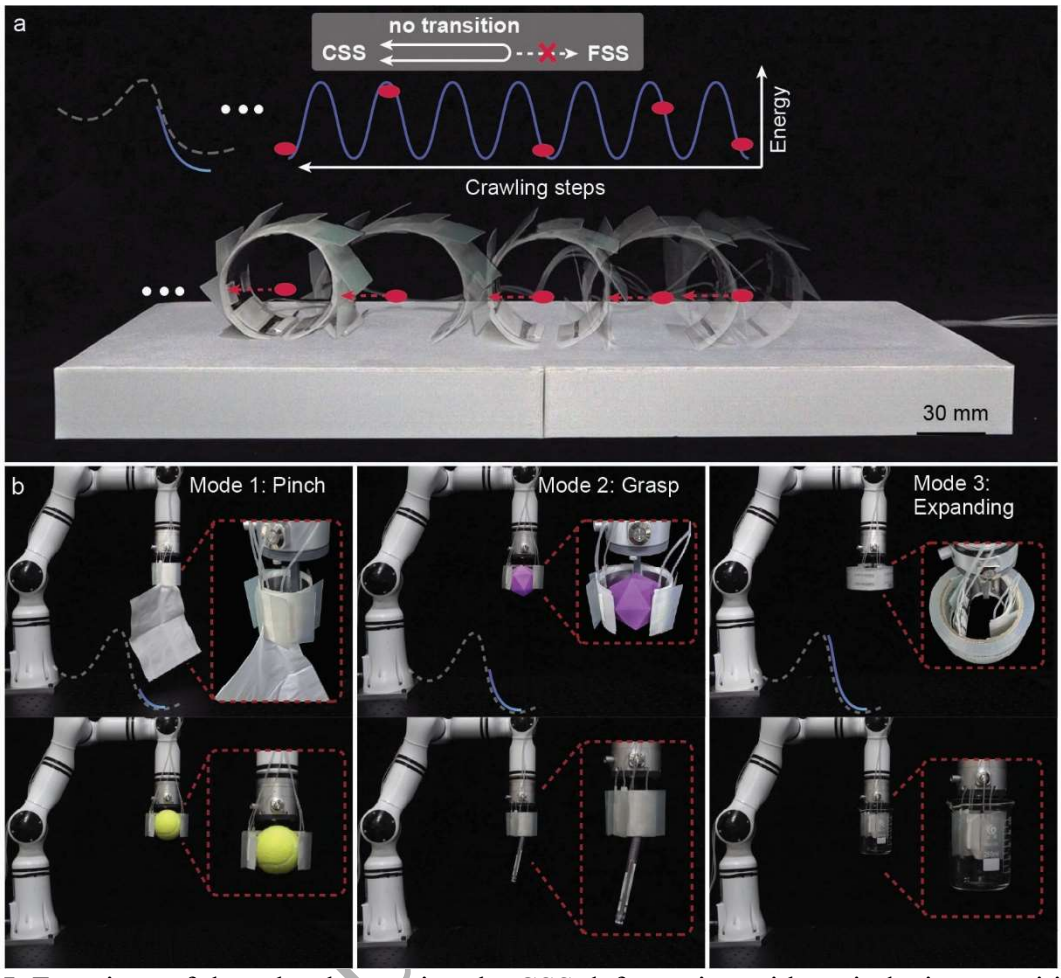


Figure 5. Functions of the robot leveraging the CSS deformation without inducing transition. The CSS configuration is relatively stable and can undergo some deformation without triggering the snap-through phenomenon. This deformation enables periodic, powerful functionality. (A) Crawling: Demonstration of ELTraBot crawling by periodically inflating and deflating UAP. (B) Multimodal gripping: The robot features three gripping modes: pinching a thin sheet of facial tissue paper, grasping an irregular-shaped ball, and expanding to hold a tape by pressing against its inner wall.

configurations. Utilizing these configurations and their transitions, our robot is capable of executing nine distinct functions to address various scenarios.

In summary, this innovative design empowers a bistable structure with continuous, reversible, and energy-landscape-traversal regions. The robot built upon this design features

ORIGINAL MANUSCRIPT

Downloaded from academic.oup.com/nsr/advance-article/doi/10.1093/nsr/nwag643/8917835 by Shanghai Jiao Tong University user on 23 October 2026

distinct configurations and transitions among them, enabling it to perform a wide spectrum of complex, multifunctional tasks. Beyond its potential to advance terrestrial, aerial, and underwater soft robotics, we believe that the ELTra bistable structure and robot will drive further innovations in robotics and foster solutions across diverse fields, including medical devices, adaptive architecture and deployable structures, sustainable robots and environmental monitoring, search and rescue operations, etc.

Despite the advantages of the ELTra mechanism and ELTraBot, several limitations remain, motivating further work. (1) The central principle of this study, modulating the energy landscape and tuning the corresponding energy barrier via external stimuli, is realized through fluidic actuation. However, it is important to emphasize that this principle is not limited to pneumatic systems. While pneumatic pressure offers a simple and highly adaptable route to redistribute strain energy, other actuation mechanisms could implement similar energy-programming concepts. For instance, dielectric elastomer actuators (DEAs) may enable instantaneous, high-frequency snap-through. Shape-memory polymers (SMPs) could trigger snap-through under thermal or photothermal stimulation. In addition, magneto-responsive materials could support remote, untethered modulation of the energy barrier via programmable magnetic fields. Although each material class involves trade-offs in response speed, energy density, and control complexity, the proposed structural and theoretical framework provides a basis for predicting and tailoring critical transition thresholds across different actuation methods. Consequently, future work may enable a new class of fast, reversible, and stimuli-responsive soft robots that leverage energy-landscape traversal for high-performance actuation in challenging and unstructured environments. (2) The model in this work explains the energetic origin and triggering tendency of these functions but does not quantitatively predict dynamic metrics such as jump velocity, impact response, rebound behaviour, or energy dissipation during collision. Future work will focus on developing a coupled dynamic model that integrates shell snap-through dynamics, pneumatic flow/compression, and contact mechanics, so that the transient behaviours of jumping and impact-resistant self-protection can be predicted more quantitatively. (3) The practical deployment of the current prototype is constrained by its tethered power supply and control architecture, since it is well recognized that a fully untethered design is the foundation for field-ready applications. For instance, integrating an onboard wireless module with a micro-pneumatic actuation system would enable the robot to operate in confined or hazardous environments, such as pipeline inspection or debris exploration. In addition, a self-contained power supply would support programmable and repeatable actuation cycles without external intervention. Nevertheless, realizing a fully untethered robot remains a significant engineering challenge, primarily because it requires miniaturizing high-pressure micro-pumps and integrating sufficiently high-capacity energy storage within strict payload and footprint constraints. Accordingly, our future work will focus on the co-design of the ELTra mechanical structure with commercially available micro-pumps and compact battery units.

METHODS

Material and Fabrication of the Robot

Materials used to fabricate the proposed robot include N70D rib weft-knit polyester fabric with double-sided TPU coating (0.2 mm), 3M very high bond (VHB) (0.5 mm), fiberglass board (FR-4), and Nylon mesh fabric (0.3 mm) for the rolling actuator, Chinese 50 steel (equivalent to AISI 1050 medium-carbon steel) bistable shell (0.2 mm), and Ergo-5800 adhesive.

ORIGINAL, UNEDITED MANUSCRIPT

Downloaded from academic.oup.com/nsr/advance-article/doi/10.1093/nsr/nwag643/8917835 by Shanghai Jiao Tong University user on 23 October 2026

Equipment to fabricate the robot includes a heat press machine (WT-90GS, Kajiang Co. Ltd.), a laser cutting machine (VLS 3.50; Universal Laser Systems), and a 3D printer (Ultimaker S3, Ultimaker Co. Ltd.).

The fabrication method of the robot is summarized as follows: laser-cut the fabric sheets, VHB tape, and FR-4 boards; seal the fabric and VHB using a heat press machine; insert and glue the silicone tubing; and bond the FR-4 boards to the bistable tape spring. The detailed fabrication process is provided in Supplementary Note 18 and Fig. S27.

Statistical Treatment and Model Parameters

All quantitative characterization experiments were performed on a single bistable-shell prototype, with three independent repeated trials (n = 3) for each test condition. Data points in all plots represent the arithmetic mean of the three replicate measurements, while error bars and shaded bands indicate the sample standard deviation (SD), which serves as a measure of measurement repeatability.

Air Sources and Pneumatic Control System

The detailed information about the hardware is as follows: air compressor, vacuum pump; PSOLs (Proportional Solenoid, ITV1030), and a stepper motor-driven electric cylinder (FSK-40J, FuYu Co. Ltd.) to regulate the pressures and air volume, respectively, which are powered by a regulated 24-V supply (GPS305D) and a microcontroller (Mega 2560, Arduino). The air pressure control also requires a digital-to-analog converter (DAC) module (PCF8591), reversing valves (0526T), and switching valves (0520D).

Characterization of Robot Locomotion

To collect the configuration of the robot during deployment and curling, we first prepared a transparent PET sheet printed with a Cartesian coordinate system. We scanned the robot's configuration using a scanner (LaserJet PRO, HP Co. Ltd.) by laterally placing the robot onto the PET sheet. Then, the digital configurations of the robot will be generated by analyzing the scanned pictures using software (MATLAB). The robot's position is obtained using a high-resolution video camera (FDR-AX700, SONY). A motor-driven (FuYu Co. Ltd.) lead screw (ShangYin Co. Ltd.) mechanism actuates the syringe to deliver precise volumetric air into UAP.

DATA AVAILABILITY

All the data supporting the findings of this study are available within the main text, its Supplementary Information, or are available from the corresponding authors upon reasonable request.

ACKNOWLEDGEMENTS

We thank Fei Mo, Zhongjing Sun, and Jing Chen for their help with the experiments, and all colleagues for their discussions. The authors also acknowledge support from the State Key Laboratory of Biomedical Imaging Science and System, and the State Key Laboratory of Mechanical System and Vibration.

FUNDING

This work was supported by the National Natural Science Foundation of China (T2522018

ORIGINAL UNEDITED MANUSCRIPT

Downloaded from academic.oup.com/nsr/advance-article/doi/10.1093/nsr/nwag643/8917835 by Shanghai Jiao Tong University user on 23 October 2026

and 52475038), the Science and Technology Commission of Shanghai Municipality (25XF3200400 and 24511103400), and the Xplorer Prize.

AUTHOR CONTRIBUTIONS

X.T. and Y.T.L. developed the overall concept and study design. Data collection and organization were performed by X.T. and Q.H.Y., who also participated in the formal analysis together with C.R.J. and D.W. The methodology was proposed by X.T., D.W., and Y.T.L., while the experiments were conducted by X.T., T.L.Z., and Y.K.J. Theory and computing were developed by Q.H.Y. and D.W. Validation of results involved Y.Y. and Y.T.L., and visualization was prepared by X.T., Q.H.Y., Y.K.J., and Y.T.L. The original manuscript was written by X.T. and Y.T.L., with subsequent review and editing by X.T., D.W., and Y.T.L. Funding for this study was secured by D.W., G.Y.G., and Y.T.L. The project was overseen by Y.T.L. and supervised by G.Y.G.

Conflict of interest statement. None declared.

REFERENCES

1. Hawkes EW, Blumenschein LH, Greer JD *et al.* A soft robot that navigates its environment through growth. *Sci Robot* 2017; **2**: eaan3028. https://doi.org/10.1126/scirobotics.aan3028.

2. Shah DS, Powers JP, Tilton LG *et al.* A soft robot that adapts to environments through shape change. *Nat Mach Intell* 2021; **3**: 51–9. https://doi.org/10.1038/s42256-020-00263-1.

3. Qing H, Guo J, Zhu Y *et al.* Spontaneous snapping-induced jet flows for fast, maneuverable surface and underwater soft flapping swimmer. *Sci Adv* 2024; **10**: eadq4222. https://doi.org/10.1126/sciadv.adq4222.

4. Rus D and Tolley MT. Design, fabrication and control of soft robots. *Nature* 2015; **521**: 467–75. https://doi.org/10.1038/nature14543.

5. Wang R, Zhang C, Zhang Y *et al.* Fast-Swimming Soft Robotic Fish Actuated by Bionic Muscle. *Soft Robot* 2024; **11**: 845–56. https://doi.org/10.1089/soro.2023.0163.

6. Chi Y, Li Y, Zhao Y *et al.* Bistable and Multistable Actuators for Soft Robots: Structures, Materials, and Functionalities. *Adv Mater* 2022; **34**: 2110384. https://doi.org/10.1002/adma.202110384.

7. Tang D, Zhang C, Pan C *et al.* Bistable soft jumper capable of fast response and high takeoff velocity. *Sci Robot* 2024; **9**: eadm8484. https://doi.org/10.1126/scirobotics.adm8484.

8. Cao Y, Derakhshani M, Fang Y *et al.* Bistable Structures for Advanced Functional Systems. *Adv Funct Mater* 2021; **31**: 2106231. https://doi.org/10.1002/adfm.202106231.

9. Gorissen B, Melancon D, Vasios N *et al.* Inflatable soft jumper inspired by shell snapping. *Sci Robot* 2020; **5**: eabb1967. https://doi.org/10.1126/scirobotics.abb1967.

10. Choi WY, Kim W, Choi JR *et al.* A hyperelastic torque-reversal mechanism for soft joints with compression-responsive transient bistability. *Sci Robot* 2025; **10**: eado7696. https://doi.org/10.1126/scirobotics.ado7696.

ORIGINAL UNEDITED MANUSCRIPT

Downloaded from academic.oup.com/nsr/advance-article/doi/10.1093/nsr/nwag643/8917835 by Shanghai Jiao Tong University user on 23 October 2026

11. Jiang L, Li B, Ma W *et al.* Electroactive Soft Bistable Actuator With Adjustable Energy Barrier and Stiffness. *IEEE Trans Robot* 2024; **40**: 472–82. https://doi.org/10.1109/TRO.2023.3331065.

12. Guo Q, Sun Y, Zhang T *et al.* Bistable Insect-Scale Jumpers with Tunable Energy Barriers for Multimodal Locomotion. *Adv Sci* 2024; **11**: 2404404. https://doi.org/10.1002/advs.202404404.

13. Rothemund P, Ainla A, Belding L *et al.* A soft, bistable valve for autonomous control of soft actuators. *Sci Robot* 2018; **3**: eaar7986. https://doi.org/10.1126/scirobotics.aar7986.

14. Zhakypov Z, Mori K, Hosoda K *et al.* Designing minimal and scalable insect-inspired multi-locomotion millirobots. *Nature* 2019; **571**: 381–6. https://doi.org/10.1038/s41586-019-1388-8.

15. Chen G, Long Y, Yao S *et al.* A non-electrical pneumatic hybrid oscillator for high-frequency multimodal robotic locomotion. *Nat Commun* 2025; **16**: 1449. https://doi.org/10.1038/s41467-025-56704-1.

16. Jiang Y, Li Y, Liu K *et al.* Ultra-tunable bistable structures for universal robotic applications. *Cell Rep Phys Sci* 2023; **4**: 101365. https://doi.org/10.1016/j.xcrp.2023.101365.

17. Jiang Y, Korpas LM, Raney JR. Bifurcation-based embodied logic and autonomous actuation. *Nat Commun* 2019; **10**: 128. https://doi.org/10.1038/s41467-018-08055-3.

18. Zhai Z, Wang Y, Lin K *et al.* In situ stiffness manipulation using elegant curved origami. *Sci Adv* 2020; **6**: eabe2000. https://doi.org/10.1126/sciadv.abe2000.

19. Yan W, Li S, Deguchi M *et al.* Origami-based integration of robots that sense, decide, and respond. *Nat Commun* 2023; **14**: 1553. https://doi.org/10.1038/s41467-023-37158-9.

20. Ramirez Serrano F, Hyun NP, Steinhardt E *et al.* A springtail-inspired multimodal walking-jumping microrobot. *Sci Robot* 2025; **10**: eadp7854. https://doi.org/10.1126/scirobotics.adp7854.

21. Song C and Lau D. Workspace-Based Model Predictive Control for Cable-Driven Robots. *IEEE Trans Robot* 2022; **38**: 2577–96. https://doi.org/10.1109/TRO.2021.3139585.

22. Hussein H, Santos JC, Izard JB *et al.* Smallest Maximum Cable Tension Determination for Cable-Driven Parallel Robots. *IEEE Trans Robot* 2021; **37**: 1186–205. https://doi.org/10.1109/TRO.2020.3043684.

23. Zhang C, Duan Y, Jiao Z *et al.* Functional Fluid-Based Soft Robotic Actuation. *Adv Mater* 2025; **37**: 2502669. https://doi.org/10.1002/adma.202502669.

24. Trumić M, Jovanović K, Fagiolini A. Decoupled nonlinear adaptive control of position and stiffness for pneumatic soft robots. *Int J Robot Res* 2021; **40**: 277–95. https://doi.org/10.1177/0278364920903787.

25. Jiang Y, Tong X, Li J *et al.* Reprogrammable Bistable Actuators for Multimodal, Fast, and Ultrasensitive Grasping. *IEEEASME Trans Mechatron* 2024; **29**: 984–94. https://doi.org/10.1109/TMECH.2023.3318976.

ORIGINAL UNEDITED MANUSCRIPT

Downloaded from academic.oup.com/nsr/advance-article/doi/10.1093/nsr/nwag643/8917835 by Shanghai Jiao Tong University user on 23 October 2026

26. Tang Y, Chi Y, Sun J *et al.* Leveraging elastic instabilities for amplified performance: Spine-inspired high-speed and high-force soft robots. *Sci Adv* 2020; **6**: eaaz6912. https://doi.org/10.1126/sciadv.aaz6912.

27. Liu Y, Pan F, Xiong F *et al.* Ultrafast Shape-Reconfigurable Chiral Mechanical Metamaterial based on Prestressed Bistable Shells. *Adv Funct Mater* 2023; **33**: 2300433. https://doi.org/10.1002/adfm.202300433.

28. Jeon J, Choi JC, Lee H *et al.* Continuous and programmable photomechanical jumping of polymer monoliths. *Mater Today* 2021; **49**: 97–106. https://doi.org/10.1016/j.mattod.2021.04.014.

29. Fan W, Shan C, Guo H *et al.* Dual-gradient enabled ultrafast biomimetic snapping of hydrogel materials. *Sci Adv* 2019; **5**: eaav7174. https://doi.org/10.1126/sciadv.aav7174.

30. Jiang C, Yu Q, Tong X *et al.* A nonlinear model for soft helical bistable structures. *Int J Mech Sci* 2025; **307**: 110899. https://doi.org/10.1016/j.ijmecsci.2025.110899.

31. Park JH, Kim YB, Jung GS *et al.* A theoretical, experimental and numerical investigation on the dynamic deployment stability of bistable composite tape springs. *Compos Struct* 2025; **372**: 119546. https://doi.org/10.1016/j.compstruct.2025.119546.

32. Zhang Z, Long Y, Chen G *et al.* Soft and lightweight fabric enables powerful and high-range pneumatic actuation. *Sci Adv* 2023; **9**: eadg1203. https://doi.org/10.1126/sciadv.adg1203.

33. Feng M, Yang D, Ren L *et al.* X-crossing pneumatic artificial muscles. *Sci Adv* 2023; **9**: eadi7133. https://doi.org/10.1126/sciadv.adi7133.

34. Wang D, Li L, Zhang B *et al.* Effect of temperature on the programmable helical deformation of a reconfigurable anisotropic soft actuator. *Int J Solids Struct* 2020; **199**: 169–80. https://doi.org/10.1016/j.ijsolstr.2020.04.028.

35. Pezzulla M, Stoop N, Steranka MP *et al.* Curvature-Induced Instabilities of Shells. *Phys Rev Lett* 2018; **120**: 048002. https://doi.org/10.1103/PhysRevLett.120.048002.

36. Jiang C, Wang D, Zhao B *et al.* Modeling and inverse design of bio-inspired multi-segment pneu-net soft manipulators for 3D trajectory motion. *Appl Phys Rev* 2021; **8**: 041416. https://doi.org/10.1063/5.0054468.

37. Lin Y, Zhang C, Tang W *et al.* A Bioinspired Stress-Response Strategy for High-Speed Soft Grippers. *Adv Sci* 2021; **8**: 2102539. https://doi.org/10.1002/advs.202102539.

38. Liu Y, Luo K, Wang S *et al.* A Soft and Bistable Gripper with Adjustable Energy Barrier for Fast Capture in Space. *Soft Robot* 2023; **10**: 77–87. https://doi.org/10.1089/soro.2021.0147.

39. Guo Q, Sun Y, Zhang T *et al.* Bistable Insect-Scale Jumpers with Tunable Energy Barriers for Multimodal Locomotion. *Adv Sci* 2024; **11**: 2404404. https://doi.org/10.1002/advs.202404404.

40. Zhang J, Yang H, He C *et al.* Instant Energy Barrier Modulation in Bistable Robotic

ORIGINAL UNEDITED MANUSCRIPT

Downloaded from academic.oup.com/nsr/advance-article/doi/10.1093/nsr/nwag643/8917835 by Shanghai Jiao Tong University user on 23 October 2026

Grippers for Compliant Triggering and Powerful Grasping. *Research* 2025; **8**: 0737. https://doi.org/10.34133/research.0737.

41. Usevitch NS, Hammond ZM, Schwager M *et al.* An untethered isoperimetric soft robot. *Sci Robot* 2020; **5**: eaaz0492. https://doi.org/10.1126/scirobotics.aaz0492.

42. Lee JY, Han S, Kim M *et al.* Variable-stiffness–morphing wheel inspired by the surface tension of a liquid droplet. *Sci Robot* 2024; **9**: eadl2067. https://doi.org/10.1126/scirobotics.adl2067.

43. Che J, Yang X, Peng J *et al.* Arc-heating actuated active-morphing insect robots. *Nat Commun* 2025; **16**: 3014. https://doi.org/10.1038/s41467-025-58258-8.

44. Jayaram K and Full RJ. Cockroaches traverse crevices, crawl rapidly in confined spaces, and inspire a soft, legged robot. *Proc Natl Acad Sci* 2016; **113**: E950–7. https://doi.org/10.1073/pnas.1514591113.

45. Wang Y, Wang Q, Liu M *et al.* Insect-scale jumping robots enabled by a dynamic buckling cascade. *Proc Natl Acad Sci* 2023; **120**: e2210651120. https://doi.org/10.1073/pnas.2210651120.

46. Han L, Si J, Zhu B *et al.* A Multidirectional Locomotion Light-Driven Soft Crawling Robot. *Adv Funct Mater* 2023; **33**: 2305046. https://doi.org/10.1002/adfm.202305046.

47. Tirado J, Do CD, Moisson de Vaux J *et al.* Earthworm-Inspired Soft Skin Crawling Robot. *Adv Sci* 2024; **11**: 2400012. https://doi.org/10.1002/advs.202400012.

48. Zhang Z, Ni X, Wu H *et al.* Pneumatically Actuated Soft Gripper with Bistable Structures. *Soft Robot* 2022; **9**: 57–71. https://doi.org/10.1089/soro.2019.0195.

49. Jain S, Dontu S, Teoh JEM *et al.* A Multimodal, Reconfigurable Workspace Soft Gripper for Advanced Grasping Tasks. *Soft Robot* 2023; **10**: 527–44. https://doi.org/10.1089/soro.2021.0225.

ORIGINAL UNEDITED MANUSCRIPT

Downloaded from academic.oup.com/nsr/advance-article/doi/10.1093/nsr/nwag643/8917835 by Shanghai Jiao Tong University user on 23 October 2026